Horizontal and vertical thermospheric cross-wind from GOCE linear and angular accelerations

Visser, T.; March, G.; Doornbos, E.; de Visser, C.; Visser, P.

DOI
10.1016/j.asr.2019.01.030

Publication date
2019

Document Version
Accepted author manuscript

Published in
Advances in Space Research

Horizontal and vertical thermospheric cross-wind from GOCE linear and angular accelerations

T. Visser[a,*], G. March[a], E. Doornbos[a], C. de Visser[a], P. Visser[a]

[a] *Delft University of Technology, Faculty of Aerospace Engineering, Kluyverweg 1, 2629HS Delft, The Netherlands.*

Abstract

Thermospheric wind measurements obtained from linear non-gravitational accelerations of the Gravity field and steady-state Ocean Circulation Explorer (GOCE) satellite show discrepancies when compared to ground-based measurements. In this paper the cross-wind is derived from both the linear and the angular accelerations using a newly developed iterative algorithm. The two resulting data sets are compared to test the validity of wind derived from angular accelerations and quantify the uncertainty in accelerometer-derived wind data. In general the difference is found to be less than 50 m/s vertically after high-pass filtering, and 100 m/s horizontally. A sensitivity analysis reveals that continuous thrusting is a major source of uncertainty in the torque-derived wind, as are the magnetic properties of the satellite. The energy accommodation coefficient is identified as a particularly promising parameter for improving the consistency of thermospheric cross-wind data sets in the future. The algorithm may be applied to obtain density and cross-wind from other satellite missions that lack accelerometer data, provided the attitude and orbit are known with sufficient accuracy.

Keywords: Thermospheric wind, Angular accelerations, Gravity Field and steady-state Ocean Circulation Explorer (GOCE), Vertical wind

*Corresponding author

Email addresses: t.visser-1@tudelft.nl (T. Visser), g.march@tudelft.nl (G. March), e.n.doornbos@tudelft.nl (E. Doornbos), c.c.devisser@tudelft.nl (C. de Visser), p.n.a.m.visser@tudelft.nl (P. Visser)

1. Introduction

The purpose of this paper is to test the possibility of obtaining in situ horizontal and vertical cross-wind estimates from satellite angular accelerations. We do so by presenting a new algorithm that extracts cross-wind from linear or angular accelerations, and applying it to measurements of the Gravity field and steady-state Ocean Circulation Explorer (GOCE). The wind measurements derived from linear and angular accelerations are compared and their sensitivity to model parameters is evaluated.

Although accelerations are an intuitive source for in situ wind observations, it has proven to be difficult to align such measurements with existing knowledge and models, as well as with remote observations such as Fabry–Perot Interferometry (FPI) (Dhadly et al., 2017, 2018). Instead of tuning the aerodynamic model of GOCE to match the ground-based observations directly, we may first find a set of model parameters for which the linear and angular acceleration data is internally consistent. This paper serves to quantify what level of accuracy can be expected from this approach, and to identify the most sensitive model parameters.

The concept of simultaneous atmospheric observations using linear and angular motion of satellites was first adopted in the paddlewheel satellite concept (Moe, 1966; Pilinski et al., 2011). For those studies the goal was to measure the absolute thermospheric density. The paddlewheel shape of the satellites ensured that aerodynamic loads would both affect the orbital and the spin motion of the body. In recent years, a number of accelerometer missions have been operated, that presented an opportunity to obtain high resolution density data (Falin et al., 1981; Bruinsma et al., 2004; Doornbos, 2011; Siemes et al., 2016; Mehta et al., 2017; March et al., 2019). The availability of cross-track accelerations has subsequently led to a large amount of horizontal cross-wind data (Sutton et al., 2005; Cheng et al., 2008; Doornbos et al., 2010), while the vertical acceleration was generally assumed too small to obtain reliable wind measurements. The horizontal wind data have been used to improve existing models (Drob et al., 2015) and to characterize thermospheric waves (Garcia et al., 2014; Gasperini et al., 2015) and wind jets (Liu et al., 2016). Although an attitude-based algorithm has been proposed by Virgili-Llop et al. (2018), all accelerometer-derived wind measurements have so far been obtained from linear accelerations.

In this work we apply the concept of simultaneous observation of linear and angular motion to a new accelerometer-based method of deriving horizontal

and vertical thermospheric cross-wind. In short the approach is as follows. The measured accelerations are used to calculate a 'measured' net force and torque acting on the satellite. Models, measurements, and housekeeping data are used to estimate forces and torques caused by solar and Earth radiation pressure and the ion thruster, and torques caused by the gravity gradient, magnetic attitude control, and other magnetic equipment in the satellite. These models for disturbance forces and torques are described extensively by Doornbos (2011) and Visser et al. (2018) respectively, and are shown to reflect all significant non-aerodynamic disturbances. The residual force and torque, obtained by subtracting the total model output from the measurement, is therefore assumed to be aerodynamic. An aerodynamic model is made to match this residual by iteratively changing the direction of the incoming flow. The wind is defined as the difference between this new flow direction and the original aerodynamic velocity. The result is a pair of separate wind data sets, one force-derived and one torque-derived. The difference between these data sets is dominated by an offset. Therefore a second overarching algorithm is used to remove the offset by iteratively changing the thruster misalignment angles and the vertical acceleration bias.

The algorithm presented in this paper can be applied to any mission for which detailed knowledge is available of either the linear or angular accelerations, or an appropriate combination thereof. It can therefore, in itself, contribute to an increase in the amount of missions deemed suitable for wind estimation. For example, the angular accelerations may be obtained from precise attitude measurements and the along-track acceleration from the orbital motion. In the GOCE case the algorithm results in two separate cross-wind data sets, one derived from linear accelerations (force-derived), the other from angular accelerations (torque-derived). By comparing the two, we identify the major error sources in accelerometer-derived wind, and quantify their impact on the wind measurements. We formulate recommendations for ground testing campaigns, operations, and documentation of future low-Earth-orbiting, accelerometer-carrying satellite missions to improve the consistency of future wind data sets.

The paper is structured as follows. First, in Section 2, we present the data sets used as inputs and highlight the changes that were made to earlier (published) versions of the force and torque models. Then the methodology is presented in Section 3. The majority of this section is dedicated to the explanation of the algorithm with which the cross-wind is obtained from residual forces and torques. In Section 4, the resulting data sets are presented and

compared, and their sensitivity to measurement errors and model parameters is evaluated in Section 5. Finally, in Section 6, conclusions are drawn regarding the consistency of accelerometer-derived cross-wind data and the value of simultaneous wind estimation from linear and angular accelerations.

2. GOCE force and torque models

The goal of the European Space Agency (ESA) GOCE mission was to map Earth's gravity field in unprecedented spatial detail. The satellite was in a near-Sun-synchronous, near-circular dusk–dawn orbit with an inclination of 96.7°. Starting at a mean altitude of 260 km at the start of the science mission in November 2009, the orbit was gradually lowered from August 2012 onwards to 229 km at the end of the mission in November 2013. An ion engine providing continuous thrust was used to create a drag-free measurement environment.

To achieve its mission objective, GOCE was equipped with a gradiometer consisting of six accelerometers positioned on the three principle axes of the satellite body, each measuring the linear acceleration along all three principle axes. The resulting 18 accelerations can be combined in specific ways to obtain the gravity gradients. By taking different combinations of the individual acceleration measurements, the linear and angular non-gravitational accelerations of the satellite body are found (Siemes et al., 2012; Stummer, 2012). The resulting data products are used in this work to derive the in situ thermospheric wind. The low orbit required for the mission results in a large aerodynamic signal. We will show in Section 4 that this even allows for vertical wind measurements on the heavily controlled pitch axis.

Even though the aerodynamic signal is large, accurate models of all other major disturbance forces and torques are required. In terms of forces this amounts to modeling the thrust, and solar, Earth albedo, and infrared radiation pressure. The first is provided as part of the housekeeping data in terms of the commanded thrust. We use the thrust command instead of the achieved thrust as it is more smooth (Wallace et al., 2011), making it more representative of the ten second intervals at which we sample the data. The latter is derived from the position of the Sun and Earth with respect to the satellite, and using ANGARA force coefficients (Doornbos, 2011; Visser et al., 2018). The sum of the models is compared to the 'measured' force, defined as the product of the interpolated mass of the satellite, and calibrated

linear accelerations obtained through the method of Visser and van den IJssel (2016).

In terms of the torques a total of five different disturbances are modeled, namely the thruster misalignment, solar, Earth albedo and infrared radiation pressure (using ANGARA torque coefficients), gravity gradient, attitude control, and magnetic torques. These models are described and validated by Visser et al. (2018). The 'measured' torque, eclipse transition model, and the aerodynamic model have however been updated. First, instead of calibrating the EGG_CGA (Electrostatic Gravity Gradiometer - Calibrated Gradiometer Angular accelerations) product, the 'measured' torque is calculated entirely from the EGG_GAR (Gradiometer Angular Rate) product (Stummer, 2012, Section 6.2). The angular acceleration is derived from this product by taking the eight point central difference of the original 1Hz signal. The result is interpolated on a 0.1Hz signal, as are all other data. Second, we replaced the geometric eclipse model by a parametrization of the physics-based SOLAARS model of Robertson et al. (2015). The parametrization, described in detail in Section 3.7 of Robertson (2015), assumes a standard atmosphere, global average cloud top height, and fixed aerosol profile. Third, we use NRLMSISE-00 densities (Picone et al., 2002) and no wind data or model to calculate the initial aerodynamic torque, to completely decouple linear and angular accelerations. Only the payload magnetic dipoles are affected by this change, as they are re-estimated using the new set of models. Fourth, the aerodynamic coefficients are obtained from a new high-fidelity geometry and aerodynamic model of GOCE using the rarefied gas simulator SPARTA (Gallis et al., 2014). This model is described in detail and compared to other existing models by March et al. (2019). We assume fully diffusive reflection with energy accommodation coefficient 0.93, in line with Sutton (2009). The energy accommodation coefficient α_E is defined e.g. in Eq. (2) of March et al. (2019), as a function of incoming and re-emitted particle temperatures, and satellite wall temperature. The proper value of the accommodation coefficient is the subject of ongoing research (e.g., Moe and Moe (2005); Pilinski et al. (2010); Mehta et al. (2013); Pilinski et al. (2013); Walker et al. (2014a,b)). The influence of this parameter on the wind data is elaborated on in Section 5, and more extensively in a future publication.

Since the publication of the GOCE torque models, the scientific data of the mission have been reprocessed to account for the quadratic calibration term of the accelerometers (Siemes, 2018). This reprocessing had no significant effect on the measured and modeled forces and torques. Only small changes

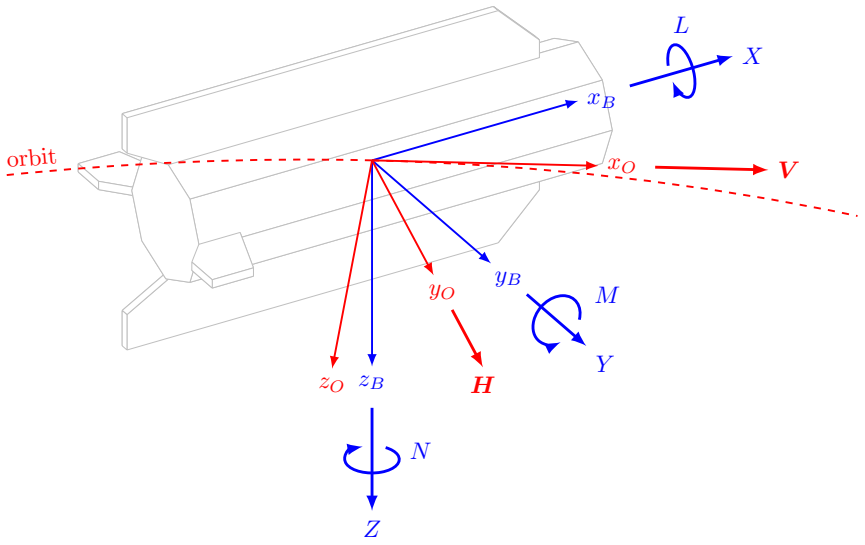

Figure 1: Definition of the force and torque components in the body (B) frame, and of the local orbit (O) frame based on the inertial velocity $\boldsymbol{V}$ and orbital angular momentum $\boldsymbol{H}$.

were found in magnetometer calibration parameters and estimated magnetic dipoles. The reprocessed data is used for all results shown in this paper.

3. Methodology

In this section we present a new algorithm that can be used to derive both horizontal and vertical cross-wind from both linear and angular accelerations. Because torques are more intuitive to work with than angular accelerations, the algorithm is set up to work with forces and torques instead. Describing forces and torques as vectors, any combination of force and torque components can be used as input. The components ate defined in the body (B) frame, as displayed in Fig. 1. In our experience, the horizontal cross-wind is observed both in the lateral body force (Y) and the yaw torque (N); the vertical wind affects both the vertical force (Z) and the pitch torque (M); the density primarily affects the longitudinal force (X). In roll (L) the aerodynamic torques are too small to yield a valuable wind or density measurement. In the remainder of this paper we mean by torque-derived wind, wind derived from longitudinal force, and pitch and yaw torques (X, M, N).

The residual forces and torques are obtained by reducing the measured forces and torques by modeled disturbances, as discussed in Section 2. It

was found that when forces and torques are mixed, scaling of the residuals is required to prevent a bias towards the force residual. Based on the mean and standard deviation of the force and torque residuals, a scale of 10 was selected to increase the weight of the torque residual. In the remainder of this section we discuss the algorithm in terms of torques only. The process is exactly the same for forces.

The algorithm is an implementation of Newton's root-finding method using numerical derivatives, and generalizes the algorithm of Doornbos et al. (2010) to the full-dimensional case. Each iteration consists of six steps, as presented in Fig. 2 and outlined below. It is initialized with the orbital velocity including co-rotation of the atmosphere and densities obtained from NRLMSISE-00.

1. Based on the (initial) aerodynamic velocity $\boldsymbol{V}_i$ the aerodynamic torque is calculated using Eq. (4) of Visser et al. (2018) (or Eq. (3.6) of Doornbos (2011) for the force equivalent). Both the aerodynamic $\boldsymbol{T}_A$ and residual torque $\boldsymbol{T}_R$ are normalized to $\hat{\boldsymbol{T}}_A$ and $\hat{\boldsymbol{T}}_R$, and the error $\Delta\boldsymbol{T}$ between the two is found.
2. The direction error is converted to an angle μ between the two torques, and the direction vector $\boldsymbol{e}$. The latter is defined as the vector perpendicular to $\hat{\boldsymbol{T}}_A$, tangential to the great circle through $\hat{\boldsymbol{T}}_A$ and $\hat{\boldsymbol{T}}_R$, centered at the center of mass of the satellite.
3. Using the Gram–Schmidt method, two directions $\boldsymbol{u}$ and $\boldsymbol{w}$ perpendicular to the current aerodynamic velocity are found. Small perturbations are made to the velocity in those directions (only drawn for $\boldsymbol{u}$ in Fig. 2) and the aerodynamic torque is recalculated and normalized.
4. The changes in aerodynamic torque direction $\partial\hat{\boldsymbol{T}}_A$ due to these velocity variations are decomposed into an angle $\partial\mu$ and the tangential $\boldsymbol{e}_u$ along the great circle through the old and new aerodynamic torque. Dividing the angle increment by the change in velocity we find approximate derivatives of these angles.
5. The derivatives are collected in a Jacobian matrix, after which the linearized system

$$\mu\boldsymbol{e} = \begin{bmatrix} \frac{\partial\mu}{\partial\boldsymbol{u}}\boldsymbol{e}_u & \frac{\partial\mu}{\partial\boldsymbol{w}}\boldsymbol{e}_w \end{bmatrix} \begin{pmatrix} a_u \\ a_w \end{pmatrix} \tag{1}$$

is solved for the velocity components a_u and a_w in a weighted least squares sense. The weights are chosen to be the inverse standard deviation of the measured torque components.

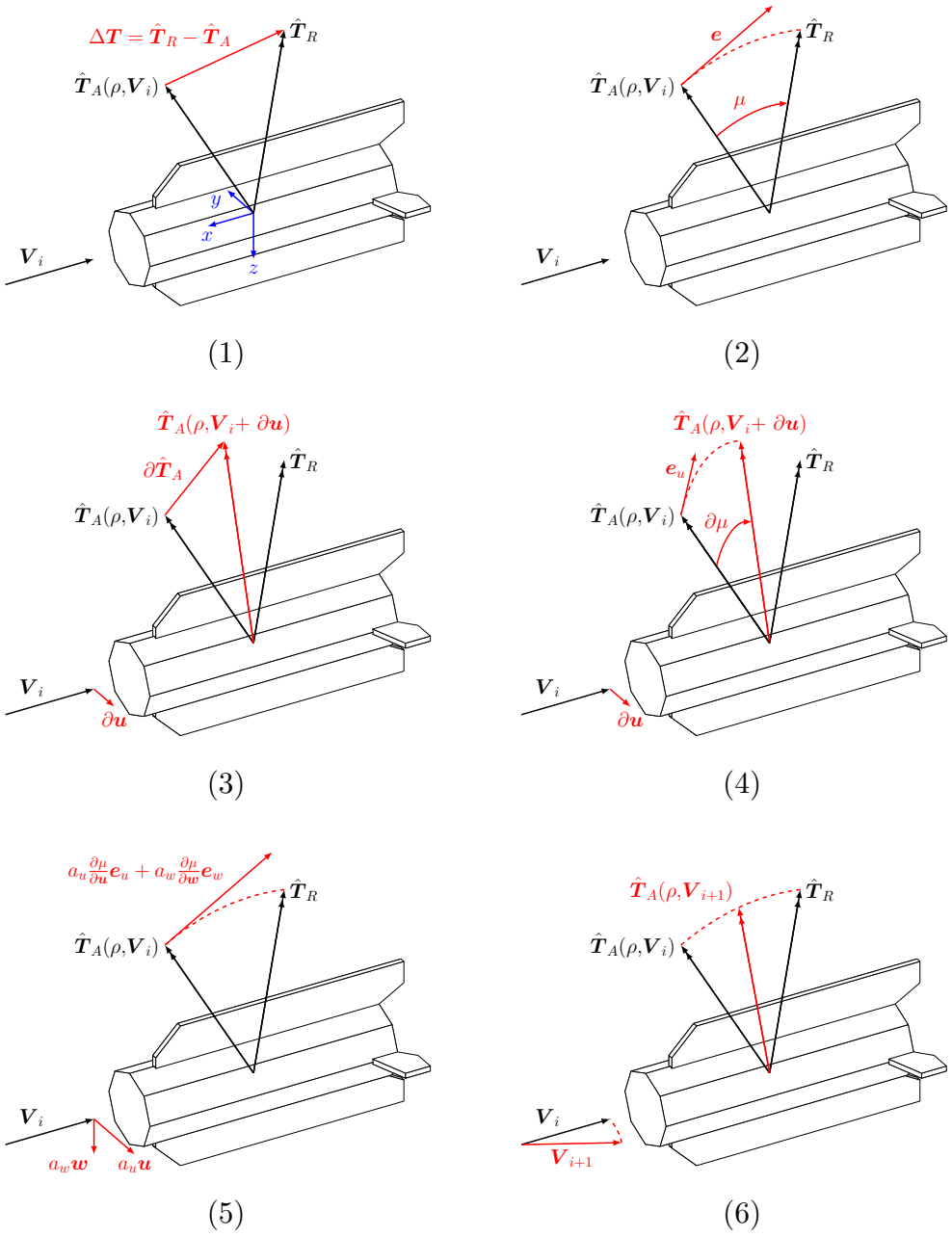

Figure 2: Schematic overview of the six steps of the algorithm to determine the wind from the torque measurements and models. The same algorithm is applied to derive wind from measured and modeled force. Note that direction vectors $\boldsymbol{e}$ and normalized torques (indicated with a hat) are drawn with different lengths to improve the clarity of the figure.

6. The velocity updates a_u and a_w are scaled with a learning rate γ_i before they are applied to their respective velocity update vectors $\boldsymbol{u}$ and $\boldsymbol{w}$. The learning rate gradually increases as $\gamma_i = \min\{0.1 + i/10, 0.9\}$, with i the iteration counter. The velocity is normalized to its original magnitude.

The algorithm normally converges in 10 iterations, using a maximum angle error $\max(\mu) < 1''$ as the stopping criterion. The wind is defined as the difference between the final aerodynamic velocity and the initial (orbital plus co-rotation) velocity. After convergence, a separate scale factor is calculated for the density at each time instant, by taking the ratio of the magnitudes of the aerodynamic and residual torque vectors.

The total (three-dimensional) wind measurements are rotated from the body (B) frame (in which they are derived, defined in blue in Fig. 1) to the local orbit (O) frame (red in Fig. 1). The horizontal cross-wind is thus defined along the orbital angular momentum vector, and the vertical wind in the nadir direction perpendicular to both the inertial velocity and orbital angular momentum vectors. The differences between the O- and B-frame are minimal, except for a rotation of 180° around the longitudinal axis. This ensures that positive vertical wind is upward. The combination of the dusk–dawn orbit configuration and the flow from the day- to the night-side of the Earth results in a predominantly negative horizontal wind in this frame.

The algorithm can only provide us with the direction of the incoming flow, not its magnitude. This implies that the wind component in the direction of the incoming flow cannot be isolated from the density estimate. By studying the wind in the orbit frame we reduce one component of the wind estimate (along-track in this case) to a minimum, while at the same time being independent of the wind direction or satellite attitude for its definition. In theory the algorithm could estimate the magnitude of the incoming flow if four or more force and torque components are combined. In practice, however, the aerodynamic force and torque models are not linearly independent in their response to flow incidence angles.

Applying the above algorithm to the entire GOCE mission, we found a strong bias towards upward wind, and an offset between cross-wind components derived from forces and those derived from torques. From the sensitivity analysis (discussed in detail in Section 5) it was concluded that both could be explained by a small adjustment of both the vertical acceleration bias and the thruster misalignment angles. Therefore these parameters were

estimated with an overarching algorithm. First, the partial derivatives of the force-derived and torque-derived wind with respect to the parameters is found from the forward difference. Then, assuming the wind is linear in the parameters, we solve for the bias and thruster angles. Finally, we estimate a single value for the bias and thruster angles for a full day of data, such that the force-derived vertical wind and the difference between force-derived and torque-derived wind (both horizontal and vertical) are minimized in a least squares sense. The influence of the energy accommodation coefficient on this estimates will be the subject of a future study.

The thrust angles are defined as displayed in Fig. 3, such that the unit thrust vector $\hat{\boldsymbol{F}}_T$ is found as

$$\hat{\boldsymbol{F}}_T = \begin{pmatrix} \cos\alpha\cos\beta \\ \sin\beta \\ \sin\alpha\cos\beta \end{pmatrix} \tag{2}$$

in the body frame. The algorithm is run for each day resulting in the daily estimates of the angles plotted in Fig. 4. While the α estimates are centered around the documented value, the β estimates assume an opposing sign. This is most likely due to the fact that the spacecraft layout had to be inverted, to match the change in the target orbit orientation when the launch was postponed. The documentation may be describing the initially intended spacecraft configuration, rather than the one that was flown. Four linear trends have been estimated for the thrust angles as a function of mean thrust level, in accordance with the documentation (Kolkmeier et al., 2008, see Table 6.6-2). They are plotted in the same figure, and listed in Table 1. The episodes were chosen based on visual inspection of Fig. 4, and constitute the time before and after August 2012 respectively, as well as the months August and November of 2012. These two months deviate from the nominal mission because of significant orbit lowering operations (GOCE Flight Control Team (HSO-OEG), 2014). To remove outliers, the weighted sum of the square distance from the fit in α (unit weight) and β (weighted ten) was calculated. The data point with the highest sum was removed, after which the linear fits were re-estimated. This process was repeated 20 times for the first nominal mission phase, four times for the second, and two times for both maneuvers, resulting in a total of 28 outliers being removed. The values in Table 1 and lines in Fig. 4 reflect the final result. Although the parameterization is based on the daily mean thrust level, the angles are calculated using the instantaneous thrust in the updated force and torque models.

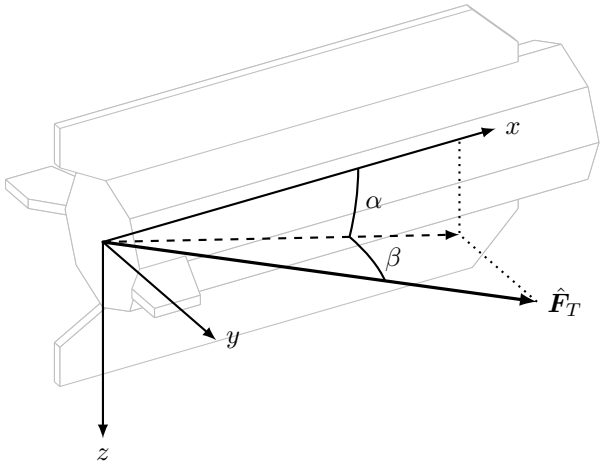

Figure 3: Definition of the thrust angles α and β for the unit thrust vector $\hat{\boldsymbol{F}}_T$ in the satellite body frame (translated to the thrust application point for clarity), with z nadir pointing.

Table 1: Linear parameterizations of the thrust angles α and β in terms of the thrust level.

	Thrust α [deg, deg/N]		Thrust β [deg, deg/N]	
Time period	Constant	Linear	Constant	Linear
2009-11-01 – 2012-07-31	-2.17	26.14	-0.01	33.88
2012-08-01 – 2012-08-31	-2.23	63.04	0.64	-104.99
2012-09-01 – 2012-10-31[a]	-2.07	12.03	0.09	11.83
2012-11-01 – 2012-12-02	-2.13	23.68	0.35	-12.90
2012-12-03 – 2013-09-30[a]	-2.07	12.03	0.09	11.83

[a] These episodes were merged to find a single parameterization.

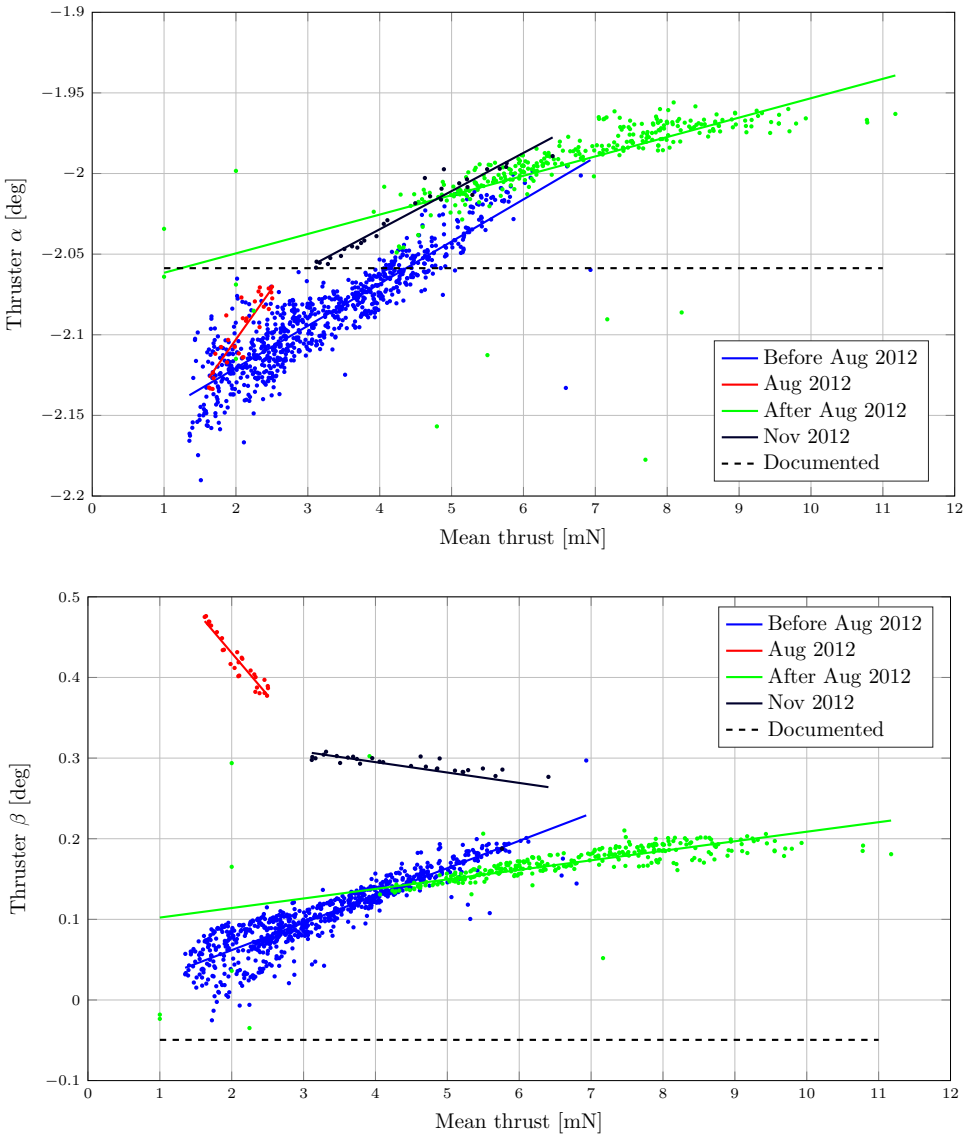

Figure 4: Daily thrust α (top) and β (bottom) estimates as a function of daily mean thrust.

Table 2: Linear parameterizations of the wind-derived vertical acceleration bias as a function of time. Time is measured in days since the start of the episode.

Time period	Constant [nm/s^2]	Linear [nm/s^2/day]
2009-11-01 – 2010-07-31	-36.48	-0.0066
2010-08-01 – 2012-07-31	-34.86	0.0037
2012-08-01 – 2012-08-31	-35.63	0.0591
2012-09-01 – 2013-09-30	-31.18	0.0169

The daily vertical acceleration bias estimates are plotted alongside the estimates from orbit determination (using the method of Visser and van den IJssel (2016) and the reprocessed GOCE data) in Fig. 5, and the linear fit parameters are listed in Table 2. Note that the wind-based estimates are significantly more consistent than the orbit-based ones. Bias estimates below -43 nm/s^2 and above -20 nm/s^2 (17% of the data points, mostly days with a lack of data) are removed before four linear trends in time are estimated. Instead of isolating the November 2012 orbit maneuver, the early part of the mission (before the summer 2010 anomaly (GOCE Flight Control Team (HSO-OEG), 2014)) is treated separately. The spread in the bias is larger for this part of the mission because of low solar activity and the resulting small aerodynamic force and torque, allowing for errors in other models to become more dominant in the derived wind.

Using the linear parameterizations for the thruster angles and the acceleration bias the thrust force and moment and the measured force are recalculated. Then the residual torque and the payload dipole estimates are updated. The updated models serve as inputs to the wind algorithm described above to obtain the force-derived and torque-derived cross-wind data sets.

4. Results

A total of four data sets result from the aforementioned approach: horizontal and vertical cross-wind derived from forces or torques. Because force modeling is significantly less complex than torque modeling, we take the force-derived wind as reference. This assumption allows us to evaluate the quality of the torque-derived wind. The validity of the horizontal force-derived wind is discussed by Dhadly et al. (2017, 2018) in a comparison with other wind observations.

A complete mission overview of the horizontal wind is plotted in Fig. 6. It

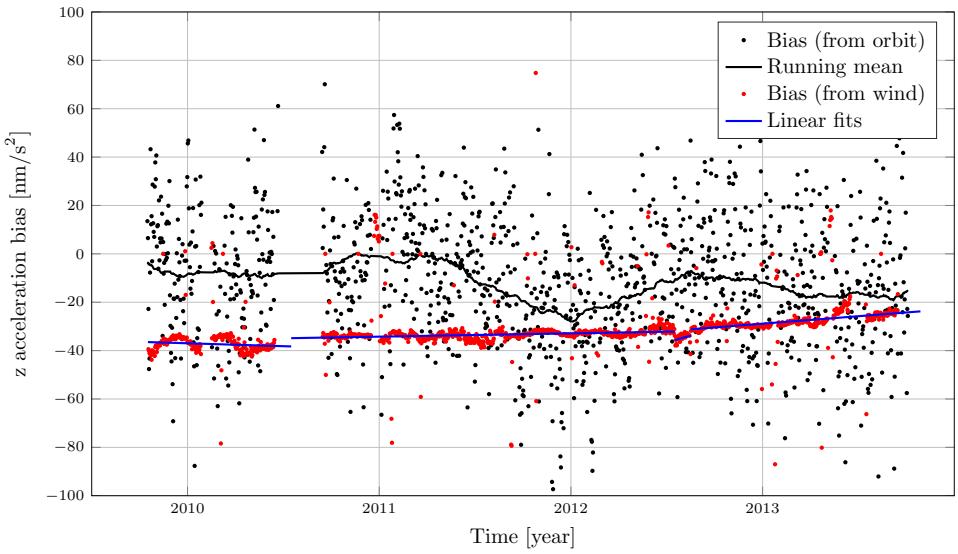

Figure 5: Daily wind-derived vertical acceleration bias estimates as a function of time along with the linear parameterizations, compared to orbit-derived biases.

shows the dependence of the horizontal wind on the argument of latitude, i.e. the progress through the orbit in degrees starting from the ascending node. The areas around the magnetic poles (around 90° argument of latitude for the North pole and 270° for the South pole) are visible as regions of increased wind and wind reversal. The dominant negative sign of the horizontal wind indicates a net flow from the day to the night side of the Earth, as should be expected. A seasonal trend is observed in the form of increased wind magnitude in the dawn sector (90° to 270° argument of latitude) of the summer hemisphere and the dusk sector of the winter hemisphere. Finally, combining the wind plots with the eclipse function in Fig. 7, a decrease in wind activity is revealed in the polar regions during eclipse, as compared to full sunlit conditions.

The difference between the two data sets, plotted in the bottom panel of Fig. 6, reveals two main patterns. First is a difference between the two hemispheres. This pattern closely follows the vertical component of the Earth's magnetic field. It could be explained by an electric dipole on the satellite in the order of 10^{-5} Cm, but no source for a sufficiently large charge has been identified so far. The second pattern takes the form of a group of once per year oscillations in argument of latitude. It follows the eclipse pattern

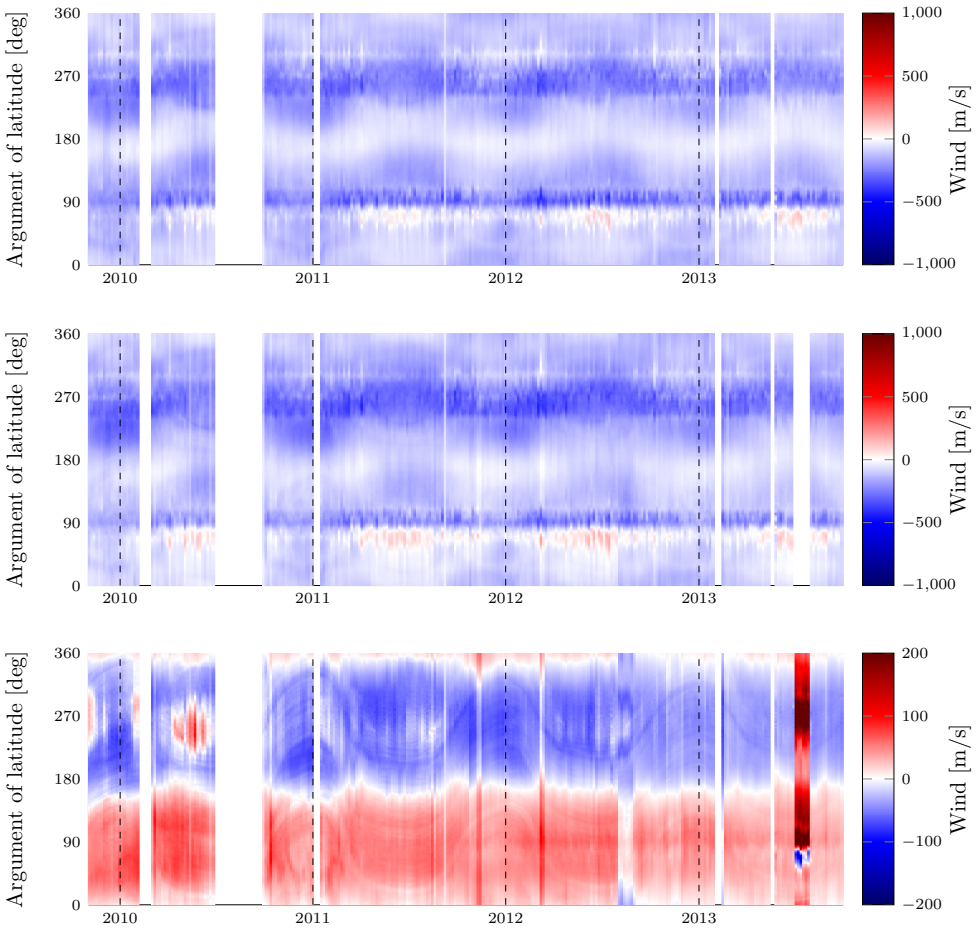

Figure 6: Horizontal wind derived from forces (top) and torques (middle), and the difference between the two (bottom), for the full mission. Note the difference in color scales.

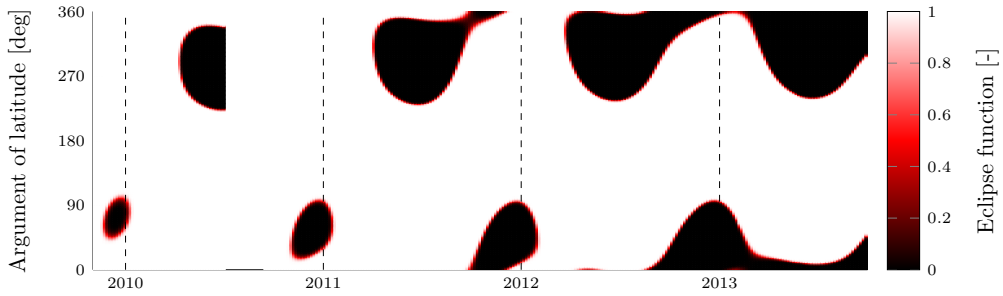

Figure 7: Eclipse function (0 in eclipse, 1 in full sunlight) for the full mission, as a function of time and argument of latitude.

Table 3: Mean (μ) and standard deviation (σ) of force- and torque-derived wind, and of the difference between the two.

	Horizontal [m/s]	Vertical [m/s]
	$\mu \pm \sigma$	$\mu \pm \sigma$
Force-derived	-128.81 ± 103.24	1.91 ± 11.56
Torque-derived	-127.35 ± 112.15	12.13 ± 70.04
Difference	1.48 ± 49.69	10.21 ± 67.85

observed in Fig. 7, implying a relation with the sunlight incidence angle. The pattern disappears inside eclipse. This error may be caused by errors in the solar radiation pressure modeling or by the unmodeled magnetic effect of currents from the solar panels, but no complete explanation has been found so far. The horizontal cross-wind data sets are compared in terms of their mean and standard deviation in Table 3. The difference between the two data sets is generally smaller than 100 m/s.

The same overview is plotted for the vertical wind in Fig. 8. The force-derived vertical wind (top panel) reveals a small consistent upward wind on the Northern hemisphere, and a small downward wind on the Southern hemisphere. The main feature however is a large amount of short-lived, small-scale peaks in the auroral zones and over the polar caps. This is consistent with previous vertical wind observations (Smith, 1998; Innis and Conde, 2002). A detailed comparison with other satellite observations will be the subject of a future publication.

The discrepancy between the two vertical wind data sets is significantly larger. This is illustrated by the similarity of the torque-derived data (middle panel) to the difference (bottom panel), which is also reflected in the mean

and standard deviation in Table 3. The largest errors in the torque-derived wind are found around the South pole (apogee) in local winter, especially early in the mission (at low solar activity); i.e. when density is low. These errors are caused by erratic behavior of the thruster at low thrust levels that is lost in the down-sampling of the data. Despite our efforts to remove any bias from the vertical wind, the mean value over the first half of 2010 remains 9 m/s upward. This may be explained by the low quality of the linear fit to the acceleration bias in Fig. 5 in this time frame. The eclipse transition patterns of Fig. 7 are clearly visible in the torque-derived vertical wind, confirming the errors related to solar radiation or solar panel currents mentioned above.

As vertical wind is generally characterized by short-lived, small-scale peaks, it is worthwhile to compare the two data sets in terms of their high frequencies only. Through trial and error we found that at frequencies above ten times orbital frequency (periods shorter than 9 minutes, spatial scales smaller than 4000 km), the two data sets show striking similarities. This is shown in Fig. 9, where the two data sets and their difference are plotted from 11:25 to 11:50 UTC on 17 March 2013, after passing them through a high-pass third-order Butterworth filter rejecting frequencies below ten times the orbital frequency. The difference is reduced to less than 50 m/s for wind values up to 200 m/s, and a strong correlation is revealed between the force- and torque-derived data.

5. Sensitivity analysis

As the algorithm output is affected by model parameters and measurement errors, the sensitivity of the wind data is evaluated for both. Uncertainty values are applied as constant positive offsets from the nominal case, except for the accommodation coefficient, which replaces the default value of 0.93. Using the new parameter value the modeled and measured force and torque are calculated anew for March 2013. This month is representative of the complete data set, but because of the lower altitude, medium-high solar activity, and equinox conditions, it lacks many of the systematic errors described in the previous section. Note that the affected torque replaces the old version in the notch-filtered residual torque (as per the terminology and methodology used by Visser et al. (2018)) without applying the notch filter to the new residual or estimating the payload dipoles again. The newly found residual force and torque are used as inputs to the wind algorithm in Section

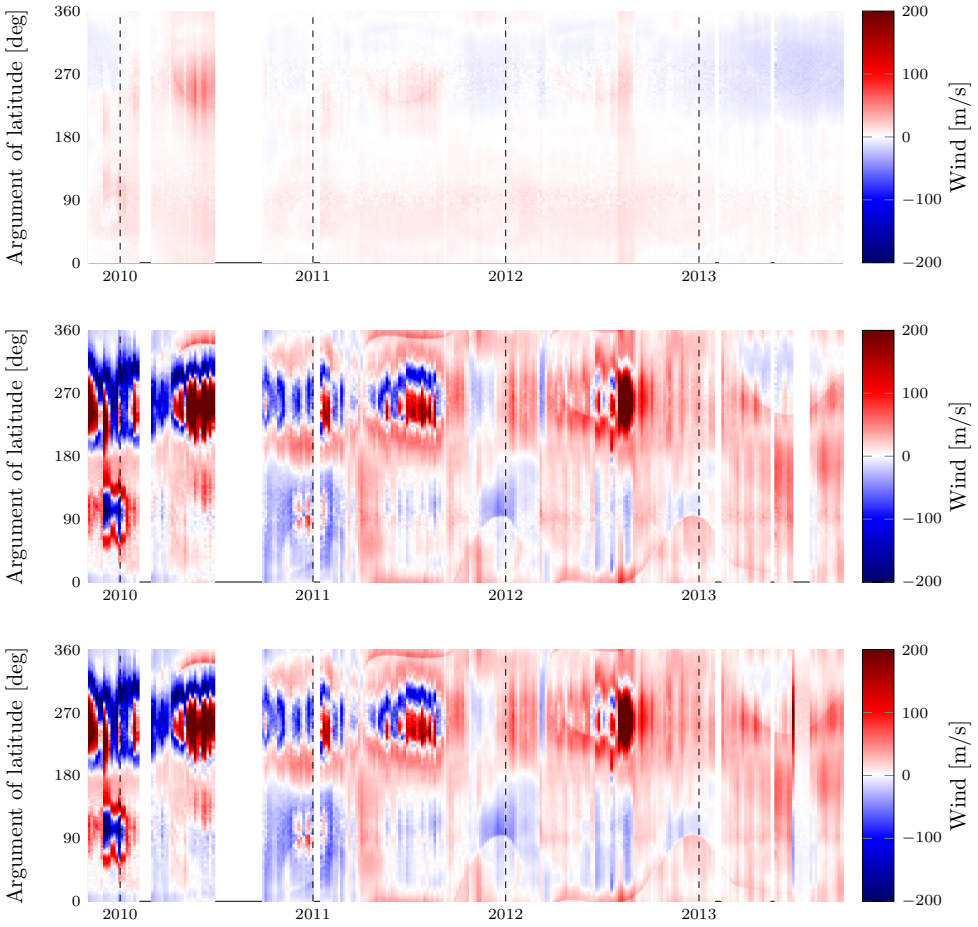

Figure 8: Vertical wind derived from forces (top) and torques (middle), and the difference between the two (bottom), for the full mission.

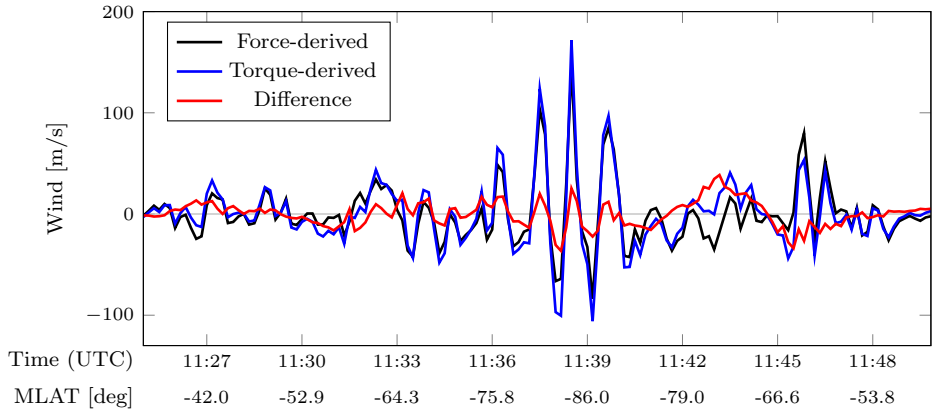

Figure 9: Time series of strong vertical wind peaks on 17 March 2013 over the South pole. Both force- and torque-derived wind are high-pass filtered to reveal their similarity above ten times the orbital frequency. Magnetic latitude (MLAT) is added for reference.

3 (Fig. 2) to find the new thermospheric wind. The sensitivity is expressed as the mean (μ) and standard deviation (σ) of the difference between the newly derived and the nominal wind. These values are calculated per wind direction (horizontal and vertical) and source data (forces F or torques T). Parameters that constitute a full 3×3 matrix (moment of inertia, magnetometer scale factor, control dipole scale factor, soft magnetic dipole) are only changed along the diagonal.

All measurements considered here are listed in Table 4. The uncertainty levels of the mass, inertia, and center of mass (CoM) are taken from the numerical precision in the GOCE Mass Properties file. For the vertical acceleration we use the root mean square error of the fit in Fig. 5 instead of the standard deviation of the orbit-derived estimates. The uncertainty in angular acceleration is obtained from the bias estimates of Visser et al. (2018), even though we no longer use those accelerations, and our current error is likely smaller. The root mean square error of the fit to the magnetometer scale factor estimates in Fig. 3 of Visser et al. (2018) is used as the magnetic field error.

For the model parameter uncertainties in Table 5 we extensively use the root mean square error of linear fits, either presented in this paper or our previous work (Visser et al., 2018). Exceptions are the thrust offset and thrust level that were taken from documentation, and the aerodynamic parameters

Table 4: Sensitivity of force-derived (F) and torque-derived (T) cross-wind to measurement errors, in terms of the mean (μ) and standard deviation (σ) of the change in wind in response to those errors, evaluated for March 2013.

		Horizontal [m/s]		Vertical [m/s]	
Parameter	Value	$\mu_F \pm \sigma_F$	$\mu_T \pm \sigma_T$	$\mu_F \pm \sigma_F$	$\mu_T \pm \sigma_T$
CoM shift x [mm]	0.5[a]	(−)±(−)	0.12±0.19	(−)±(−)	−0.34±0.05
CoM shift y [mm]	0.5[a]	(−)±(−)	−0.00±0.00	(−)±(−)	−0.00±0.00
CoM shift z [mm]	0.5[a]	(−)±(−)	0.00±0.00	(−)±(−)	−0.00±0.00
Roll bias [arcsec]	3[b]	−0.00±0.00	0.00±0.01	0.00±0.00	0.00±0.00
Pitch bias [arcsec]	3[b]	−0.00±0.00	−0.00±0.00	−0.11±0.00	0.31±0.15
Yaw bias [arcsec]	3[b]	0.11±0.00	0.11±0.00	−0.00±0.00	0.00±0.00
Inertia x [kgm^2]	0.05[a]	(−)±(−)	0.00±0.00	(−)±(−)	−0.00±0.00
Inertia y [kgm^2]	0.05[a]	(−)±(−)	−0.00±0.00	(−)±(−)	−0.00±0.00
Inertia z [kgm^2]	0.05[a]	(−)±(−)	0.00±0.01	(−)±(−)	0.00±0.00
Mass [kg]	0.0005[a]	−0.00±0.00	(−)±(−)	0.00±0.00	(−)±(−)
Lin. acc. x [nm/s^2]	0.3[c]	−0.00±0.01	(−)±(−)	0.00±0.00	(−)±(−)
Lin. acc. y [nm/s^2]	7[c]	−4.31±1.46	(−)±(−)	0.02±0.03	(−)±(−)
Lin. acc. z [nm/s^2]	3[d]	−0.01±0.02	(−)±(−)	−2.79±0.93	(−)±(−)
Ang. rate x [nrad/s]	10[b]	(−)±(−)	−0.05±0.02	(−)±(−)	0.00±0.00
Ang. rate y [nrad/s]	10[b]	(−)±(−)	0.00±0.00	(−)±(−)	−0.00±0.00
Ang. rate z [nrad/s]	10[b]	(−)±(−)	−0.00±0.00	(−)±(−)	0.00±0.00
Ang. acc. x [nrad/s^2]	4.2[e]	(−)±(−)	−0.01±0.01	(−)±(−)	−0.24±0.08
Ang. acc. y [nrad/s^2]	0.29[e]	(−)±(−)	0.00±0.02	(−)±(−)	−2.23±0.77
Ang. acc. z [nrad/s^2]	4[e]	(−)±(−)	18.91±6.50	(−)±(−)	−0.49±0.34
Magn. scale x [%]	0.1[e]	(−)±(−)	−0.00±0.03	(−)±(−)	−0.02±0.15
Magn. scale y [%]	0.1[e]	(−)±(−)	−0.00±0.06	(−)±(−)	0.00±0.01
Magn. scale z [%]	0.1[e]	(−)±(−)	0.00±0.00	(−)±(−)	−0.01±0.46

[a] Numerical precision in GOCE Mass Properties file.
[b] Stummer (2012).
[c] Visser and van den IJssel (2016).
[d] Root mean square error of fit, this paper.
[e] Root mean square error of fit, Visser et al. (2018).

(accommodation coefficients, specular fraction, atmospheric and wall temperature, and flow speed) that were chosen based on existing knowledge. A wide range of accommodation coefficients is considered, as its value is widely debated. The specular fraction is generally expected to be small, in the order of a few percent (Gregory and Peters, 1987). The temperature deviations were chosen significantly larger than to be expected. With flow speed we mean the magnitude of the velocity vector. Since this magnitude is kept constant in the cross-wind algorithm, this effectively reflects a constant along-track (meridional) head-wind of 200 m/s.

More than half of the parameters listed in Tables 4 and 5 affect only the torque-derived wind. On top of that the thrust angles produce significantly larger offsets in torque-derived wind than in their force-derived counterparts. This confirms our hypothesis that force modeling is less error-prone, and the force-derived wind is thus likely closer to the true wind. We discuss the four most prominent parameters in more detail below. Their effect on the wind data is plotted against magnetic latitude in Fig. 10.

First and foremost, the thruster misalignment plays a central role. From Table 5 and Fig. 10, we conclude that thrust angle α causes almost purely an offset in vertical wind, and thrust angle β in horizontal wind. The large discrepancy in sensitivity of the two data sets makes this an ideal parameter to improve their consistency. Note that the mean and standard deviation in Table 5 are computed for an error of 0.02° (the maximum root mean square error of the fits in Fig. 4), whereas a maximum error of 0.9° is reported by Kolkmeier et al. (2008). For such values of thruster misalignment the wind offsets reach values in excess of 1000 m/s. An offset in the thrust application point has a similar effect on the torque-derived wind, but its maximum magnitude is much smaller.

Second, the longitudinal component of the spacecraft magnetic dipole has a significant influence on the torque-derived wind. The vertical wind is affected the most, because of the large influence of magnetic torques on the pitch axis (Visser et al., 2018). The difference is the largest at the magnetic poles, due to the orientation of the magnetic field.

Third, the energy accommodation coefficient is changed. Note that we choose a small change of only 0.03 in Fig. 10 to compare it to the specular fraction hereafter. The parameter has by far the strongest impact of all parameters on the force-derived horizontal wind, and a large impact on the torque-derived horizontal wind. Comparing the trend in the nominal wind and the difference, we may conclude that the accommodation coefficient pri-

Table 5: Sensitivity of force-derived (F) and torque-derived (T) cross-wind to model parameters, in terms of the mean (μ) and standard deviation (σ) of the change in wind in response to changing those parameters, evaluated for March 2013.

		Horizontal [m/s]		Vertical [m/s]	
Parameter	Value	$\mu_F \pm \sigma_F$	$\mu_T \pm \sigma_T$	$\mu_F \pm \sigma_F$	$\mu_T \pm \sigma_T$
Thrust offset x [mm]	1.6[a]	(−)±(−)	−0.05±0.01	(−)±(−)	0.96±0.03
Thrust offset y [mm]	1.6[a]	(−)±(−)	17.05±0.59	(−)±(−)	−0.44±0.23
Thrust offset z [mm]	1.6[a]	(−)±(−)	−0.03±0.18	(−)±(−)	27.50±0.70
Thrust angle α [deg]	0.02[b]	0.00±0.01	−0.02±0.10	1.99±0.01	15.61±0.40
Thrust angle β [deg]	0.02[b]	−1.31±0.04	−9.68±0.35	0.00±0.01	0.25±0.13
Thrust level [%]	1[c]	0.55±1.27	0.70±1.21	−2.08±0.24	0.61±0.39
Dipole x [Am^2]	0.13[d]	(−)±(−)	−0.72±1.61	(−)±(−)	2.24±15.02
Dipole y [Am^2]	0.043[d]	(−)±(−)	−0.01±1.21	(−)±(−)	0.01±0.04
Dipole z [Am^2]	0.051[d]	(−)±(−)	−0.00±0.01	(−)±(−)	−0.02±2.33
Control dipole x [%]	0.96[d]	(−)±(−)	−0.32±1.07	(−)±(−)	0.92±10.16
Control dipole y [%]	1.93[d]	(−)±(−)	−0.16±0.52	(−)±(−)	0.00±0.02
Control dipole z [%]	1.72[d]	(−)±(−)	0.00±0.02	(−)±(−)	−0.22±2.57
Soft dipole x [Am^2/T]	1338[d]	(−)±(−)	−0.02±0.24	(−)±(−)	−0.04±1.88
Soft dipole y [Am^2/T]	1096[d]	(−)±(−)	0.02±0.20	(−)±(−)	0.00±0.01
Soft dipole z [Am^2/T]	683[d]	(−)±(−)	0.00±0.01	(−)±(−)	0.02±0.96
Accommodation [-]	0.6	13.13±34.80	0.37±32.01	−2.54±4.18	1.95±2.13
Accommodation [-]	0.8	7.85±20.86	0.28±19.06	−1.42±2.35	1.05±1.19
Accommodation [-]	0.9	2.57±6.85	0.11±6.22	−0.44±0.73	0.31±0.37
Accommodation [-]	1	−14.01±38.77	−0.88±33.81	1.94±6.49	−1.36±1.68
Specular frac. [-]	0.01	−0.11±0.30	1.31±0.46	0.06±0.10	0.16±0.25
Specular frac. [-]	0.02	−0.23±0.60	2.61±0.92	0.12±0.21	0.32±0.51
Specular frac. [-]	0.03	−0.34±0.90	3.90±1.37	0.18±0.32	0.48±0.78
Atmospheric temp. [K]	200	−0.45±0.63	−1.53±1.45	0.06±0.13	0.65±0.65
Wall temp. [K]	200	0.49±1.30	−0.00±1.18	−0.09±0.14	0.06±0.07
Flow speed [m/s]	200	−3.10±2.76	−2.80±2.60	−0.07±0.27	0.24±0.60

[a] Kolkmeier et al. (2008).
[b] Root mean square error of fit, this paper.
[c] Wallace et al. (2011).
[d] Root mean square error of fit, Visser et al. (2018).

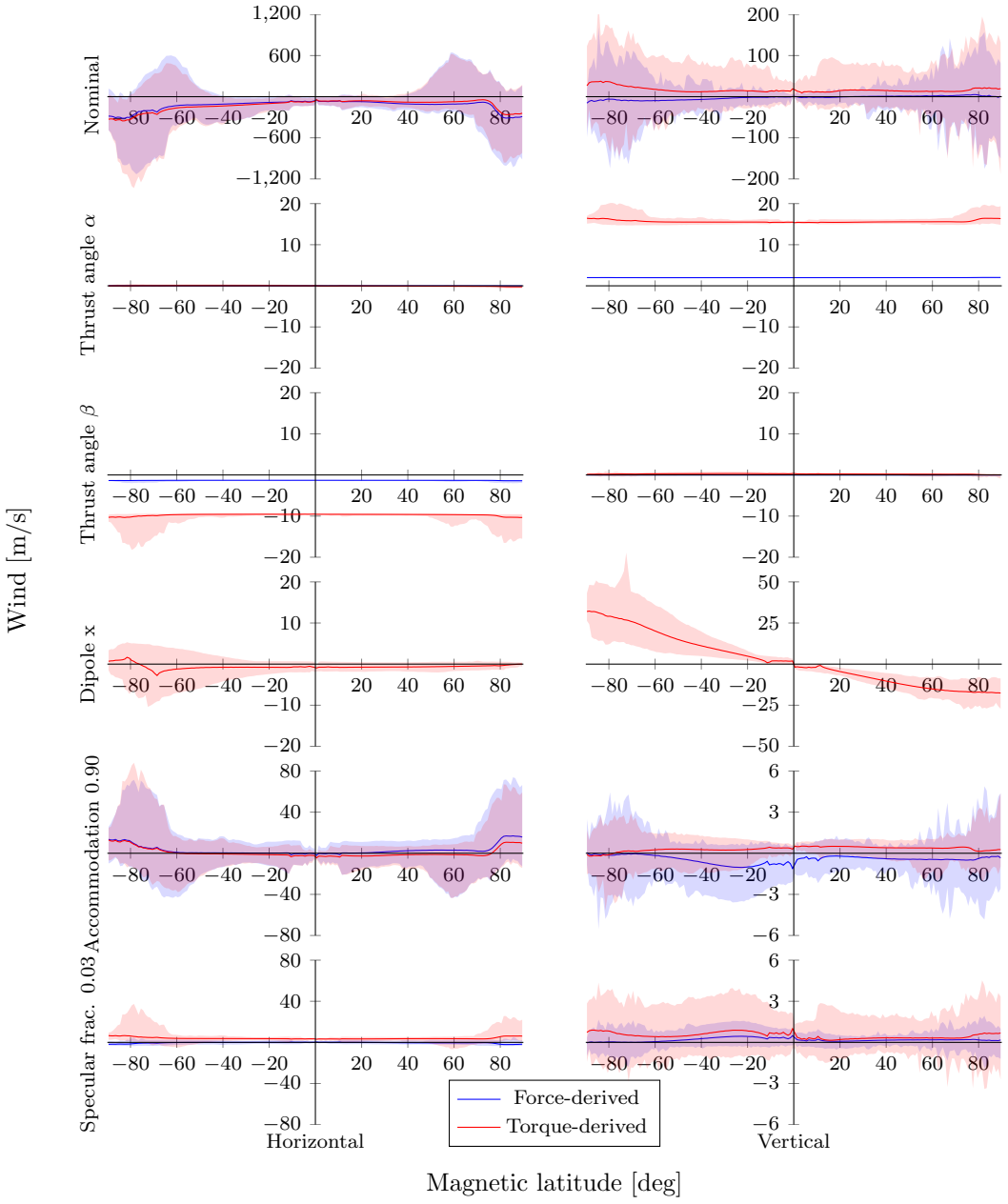

Figure 10: Horizontal (left) and vertical (right) wind difference from nominal due to a selection of model parameters from Table 5, in terms of min-mean-max over one degree magnetic latitude bins for March 2013. Note the different limits on the vertical axes.

marily scales the horizontal wind. This specific pattern was also observed by Dhadly et al. (2018) (see Fig. 2), who assumed it was a latitude-dependent offset. The vertical wind is less sensitive to the accommodation coefficient. A future study will focus on the effect of accommodation on the consistency of estimated parameters and the GOCE wind data.

Finally the specular fraction of the particle–surface interaction is investigated. The increase from 0 to 3% causes a change in horizontal wind seven times smaller than a similar adaptation of energy accommodation (from 0.93 to 0.9), judging from the standard deviations in Table 5. On top of that, it causes a slight offset in torque-derived horizontal wind, which is not observed in the force-derived wind. The overall trend of the difference is similar to that of the nominal wind. The difference in sensitivity between specular fraction and accommodation coefficient can at least in part be explained by the non-linear relation between these parameters and the aerodynamic model coefficients. At higher values of accommodation, the change in force and moment coefficients is more steep, eventually resulting in a steeper change in wind.

6. Conclusion

Comparing the cross-wind data sets presented in this paper, taking into account the required effort to arrive at the current model fidelity, we conclude that although it is possible to obtain cross-wind from angular acceleration measurements, it is highly impractical. In the specific case of GOCE the most problematic model parameter is the thruster misalignment. The extreme sensitivity to these angles forces us to use the force-derived wind measurements to tune the torque-derived ones. This fact implies that satellites that use continuous thrusting are not suitable for deriving wind purely from attitude motion. More generally for low-Earth-orbiting accelerometer missions currently in use, the knowledge of the magnetic properties of the satellite is likely insufficient to do without a dipole estimation procedure like the one of Visser et al. (2018). Although these estimates have greatly improved the result, the similarity of the difference between the two wind data sets to the vertical component of the Earth's magnetic field implies that some interaction between the magnetic field and the satellite remains unmodeled. This implies that we still lack knowledge of the magnetic and electronic properties of GOCE. Note that we have not been able to obtain magnetic properties as a function of large internal currents for GOCE in

the past (Visser et al., 2018). Later attempts to explain the difference by satellite charging, or static charges in the ion engine, have failed because the required charges were several orders of magnitude higher than anticipated. We conclude that if accurate data is to be obtained from the attitude motion of future satellites, a complete magnetic dipole budget is required, including current loops and electrically charged elements.

The difficulties described above mostly pertain to the lower frequencies. These are also the frequencies at which the estimation of magnetic dipoles, thruster misalignment angles, and acceleration bias have their primary effect. Horizontal wind errors are dominated by a once-per-orbit signal, and at frequencies above ten times orbital frequency the force- and torque-derived vertical cross-winds show a strong correlation. We may conclude that the force-derived wind is thus internally validated at frequencies above ten times orbital frequency by the torque-derived data. At the same time the mean vertical wind cannot be determined from the GOCE accelerometer data alone.

This form of internal validation of the force-derived wind is also the true value of simultaneous wind observations from linear and angular accelerations. The total set of estimated model parameters provides us with the opportunity to test the consistency of wind measurements without the need for other measurement sources. Instead of tuning aerodynamic model parameters (such as the energy accommodation coefficient) to match other models and observations, we may look for parameters that provide the most consistent estimates of magnetic, thruster, and calibration parameters, as well as consistency between force- and torque-derived wind. From the sensitivity analysis we have strong indications that lowering the accommodation coefficient from its current value of 0.93 will improve at least the latter.

A similar simultaneous estimation of the density using GOCE linear and angular acceleration data is impossible. Due to the satellite's geometric design the aerodynamic response in roll is insufficient to be used in the presented algorithm, reducing the number of independent measurements to five. Horizontal wind can be obtained from the lateral force or the yaw moment, vertical wind from the vertical force or the pitch moment, neutral density only from the longitudinal force. If a simultaneous density estimation is desired in a future mission, the paddlewheel concept could be applied to the GOCE design by rotating the fins accordingly.

Taking into account above-mentioned limitations, one particularly interesting application for the presented algorithm is the Swarm constellation. Due to limited reliability of the accelerometer data of these satellites, hori-

zontal wind data may not be obtained from the linear accelerations (Siemes et al., 2016). However, assuming that the yaw rate and acceleration can be obtained from the precise attitude data of the star cameras, the yaw torque may replace side force as a potential source for horizontal wind data. As the Swarm satellites are intended for high-accuracy measurements of the Earth's magnetic field, the magnetic properties of these satellites are well known and documented. On top of that, the Swarm satellites do not use continuous thrusting, removing the largest uncertainties from the torque modeling process. A detailed investigation into the housekeeping data and attitude motion of the Swarm satellites is required to test this hypothesis.

Acknowledgements

The authors would like to thank ESA, and specifically Micheal Fehringer, Björn Fromknecht, and Rune Floberghagen, for their support in navigating the data (access may be requested at https://earth.esa.int/web/guest/-/goce-data-access-7219; the GOCE Mass Properties file is available at https://earth.esa.int/web/guest/-/goce-mass-property-file-8276) and documentation (available through personal communication) required for this study. We also thank Robbie Robertson for kindly providing his parametrized eclipse transition model.

References

Bruinsma, S., Tamagnan, D., Biancale, R., 2004. Atmospheric densities derived from CHAMP/STAR accelerometer observations. Planetary and Space Science 52, 297–312, doi: 10.1016/j.pss.2003.11.004.

Cheng, M., Tapley, B. D., Bettadpur, S., Ries, J. C., 2008. Determination of thermospheric winds from GRACE accelerometer data. In: Advances in the Astronautical Sciences. Vol. 130. pp. 1181–1192.

Dhadly, M., Emmert, J., Drob, D., Conde, M., Doornbos, E., Shepherd, G., Makela, J., Wu, Q., Niciejewski, R., Ridley, A., 2017. Seasonal dependence of northern high-latitude upper thermospheric winds: A quiet time climatological study based on ground-based and space-based measurements. Journal of Geophysical Research: Space Physics 122 (2), 2619–2644, doi: 10.1002/2016JA023688.

Dhadly, M. S., Emmert, J. T., Drob, D. P., Conde, M. G., Doornbos, E. N., Shepherd, G. G., Makela, J. J., Wu, Q., Nieciejewski, R. J., Ridley, A. J., 2018. Seasonal dependence of geomagnetic active-time northern high-latitude upper thermospheric winds. Journal of Geophysical Research: Space Physics 123 (1), 739–754, doi: 10.1002/2017JA024715.

Doornbos, E., 2011. Thermospheric Density and Wind Determination from Satellite Dynamics. Ph.D. thesis, Delft University of Technology, Delft, The Netherlands, isbn: 978-90-9026051-8.

Doornbos, E., van den IJssel, J., Lühr, H., Förster, M., Koppenwallner, G., 2010. Neutral density and crosswind determination from arbitrarily oriented multiaxis accelerometers on satellite. Journal of Spacecraft and Rockets 47 (4), 580–589, doi: 10.2514/1.48114.

Drob, D. P., Emmert, J. T., Meriwether, J. W., Makela, J. J., Doornbos, E., Conde, M., Hernandez, G., Noto, J., Zawdie, K. A., McDonald, S. E., Huba, J. D., Klenzing, J. H., 2015. An update to the Horizontal Wind Model (HWM): the quiet time thermosphere. Earth and Space Science 2 (7), 301–319, doi: 10.1002/2014EA000089.

Falin, J. L., Barlier, F., Kockarts, G., 1981. Densities from the CACTUS accelerometer as an external test of the validity of the thermospheric models. Advances in Space Research 1 (12), 221–225, doi: 10.1016/0273-1177(81)90436-1.

Gallis, M. A., Torczynski, J. R., Plimpton, S. J., Rader, D. J., Koehler, T., 2014. Direct simulation Monte Carlo: the quest for speed. In: Fan, J. (Ed.), Proceedings of the 29th International Symposium on Rarefied Gas Dynamics. Vol. 1628. AIP Publishing, pp. 27–36, doi: 10.1063/1.4902571.

Garcia, R., Doornbos, E., Bruinsma, S., Hebert, H., 2014. Atmospheric gravity waves due to the Tohoku-Oki tsunami oserved in the thermosphere by GOCE. Journal of Geophysical Research: Atmospheres 119 (8), 4498–4506, doi: 10.1002/2013JD021120.

Gasperini, F., Forbes, J. M., Doornbos, E. N., Bruinsma, S. L., 2015. Wave coupling between the lower and middle thermosphere as viewed from TIMED and GOCE. Journal of Geophysical Research: Space Physics 120 (7), 5788–5804, doi: 10.1002/2015JA021300.

GOCE Flight Control Team (HSO-OEG), 2014. GOCE End-of-Mission Operations Report. Tech. Rep. GO-RP-ESC-FS-6268.

Gregory, J. C., Peters, P. N., 1987. A measurement of the angular distribution of 5 eV atomic oxygen scattered off a solid surface in Earth orbit. In: Boffi, V., Cercignani, C. (Eds.), Proceedings of the 15th International Symposium of Rarefied Gas Dynamics, Grado, Italy. Vol. 2. B. G. Teubner, Stuttgart, Germany, pp. 644–654.

Innis, J. L., Conde, M., 2002. High-latitude thermospheric vertical wind activity from Dynamics Explorer 2 Wind and Temperature Spectrometer observations: Indications of a source region for polar cap gravity waves. Journal of Geophysical Research 107 (A8, 1172), 11–1–11–17, doi: 10.1029/2001JA009130.

Kolkmeier, A., Präger, G., Möller, P., Strandberg, T., Kempkens, K., Stark, J., Gessler, L., Hienerwadel, K. O., 2008. GOCE - DFAC Interface Control Document. Tech. Rep. GO-IC-ASG-0005_12, EADS Astrium.

Liu, H., Doornbos, E., Nakashima, J., 2016. Thermospheric wind observed by GOCE: Wind jets and seasonal variations. Journal of Geophysical Research: Space Physics 121 (7), 6901–6913, doi: 10.1002/2016JA022938.

March, G., Doornbos, E. N., Visser, P. N. A. M., 2019. High-fidelity geometry models for improving the consistency of CHAMP, GRACE, GOCE, and Swarm thermospheric density data sets. Advances in Space Research 63 (1), 213–238, doi: 10.1016/j.asr.2018.07.009.

Mehta, P. M., McLaughlin, C. A., Sutton, E. K., 2013. Drag coefficient modeling for GRACE using Direct Simulation Monte Carlo. Advances in Space Research 52 (12), 2035–2051, doi: 10.1016/j.asr.2013.08.033.

Mehta, P. M., Walker, A. C., Sutton, E. K., Godinez, H. C., 2017. New density estimates derived using accelerometers on board the CHAMP and GRACE satellites. Space Weather 15 (4), 558–576, doi: 10.1002/2016SW001562.

Moe, K., 1966. Absolute atmospheric densities determined from the spin and orbital decays of explorer VI. Planetary and Space Science 14 (11), 1065–1075, doi: 10.1016/0032-0633(66)90022-5.

Moe, K., Moe, M. M., 2005. Gas–surface interactions and satellite drag coefficients. Planetary and Space Science 53 (8), 793–801, doi: 10.1016/j.pss.2005.03.005.

Picone, J. M., Hedin, A. E., Drob, D. P., Aikin, A. C., 2002. NRLMSISE-00 empirical model of the atmosphere: statistical comparisons and scientific issues. Journal of Geophysical Research: Space Physics 107 (A12), doi: 10.1029/2002JA009430.

Pilinski, M., Argrow, B., Palo, S., 2010. Semiempirical model for satellite energy-accommodation coefficients. Journal of Spacecraft and Rockets 47 (6), 951–956, doi: 10.2514/1.49330.

Pilinski, M., Moe, K., Palo, S., Argrow, B., 2011. Measuring absolute thermospheric densities and accommodation coefficients using paddlewheel satellites: past findings, present uses, and future mission concepts. Journal of the Astronautical Sciences 58 (3), 531–549, doi: 10.1007/BF03321184.

Pilinski, M. D., Argrow, B. M., Palo, S. E., Bowman, B. R., 2013. Semiempirical satellite accommodation model for spherical and randomly tumbling objects. Journal of Spacecraft and Rockets 50 (3), 556–571, doi: 10.2514/1.A32348.

Robertson, R., Flury, J., Bandikova, T., Schilling, M., 2015. Highly physical penumbra solar radiation pressure modeling with atmospheric effects. Celestial Mechanics and Dynamical Astronomy 123 (2), 169–202, doi: 10.1007/s10569-015-9637-0.

Robertson, R. V., 2015. Highly Physical Solar Radiation Pressure Modeling During Penumbra Transitions. Ph.D. thesis, Virginia Polytechnic Institute and State University, Blacksburg (VA), United States.

Siemes, C., 2018. Improving GOCE cross-track gravity gradients. Journal of Geodesy 92 (1), 33–45, doi: 10.1007/s00190-017-1042-x.

Siemes, C., De Teixeira Da Encarnação, J., Doornbos, E., Van Den IJssel, J., Kraus, J., Pereštý, R., Grunwaldt, L., Apelbaum, G., Flury, J., Holmdahl Olsen, P. E., 2016. Swarm accelerometer data processing from raw accelerations to thermospheric neutral densities 2. Aeronomy Swarm science results after two years in space. Earth, Planets and Space 68 (1), 92, doi: 10.1186/s40623-016-0474-5.

Siemes, C., Haagmans, R., Kern, M., Plank, G., Floberghagen, R., 2012. Monitoring GOCE gradiometer calibration parameters using accelerometer and star sensor data: methodology and first results. Journal of Geodesy 86 (8), 629–645, doi: 10.1007/s00190-012-0545-8.

Smith, R. W., 1998. Vertical winds: a tutorial. Journal of Atmospheric and Solar-Terrestrial Physics 60, 1425–1434, doi: 10.1016/S1364-6826(98)00058-3.

Stummer, C., 2012. Gradiometer Data Processing and Analysis. Ph.D. thesis, Technische Universität München, Munich, Germany.

Sutton, E. K., 2009. Normalized force coefficients for satellites with elongated shapes. Journal of Spacecraft and Rockets 46 (1), doi: 10.2514/1.40940.

Sutton, E. K., Forbes, J. M., Nerem, R. S., 2005. Global thermospheric neutral density and wind response to the severe 2003 geomagnetic storms from CHAMP accelerometer data. Journal of Geophysical Research: Space Physics 110 (A9), doi: 10.1029/2004JA010985.

Virgili-Llop, J., Roberts, P., Hao, Z., 2018. Using the attitude response of aerostable spacecraft to measure thermospheric wind. CEAS Space Journal 10 (1), 101–113, doi: 10.1007/s12567-017-0153-9.

Visser, P., van den IJssel, J., 2016. Calibration and validation of individual GOCE accelerometers by precise orbit determination. Journal of Geodesy 90, 1–13, doi: 10.1007/s00190-015-0850-0.

Visser, T., Doornbos, E., de Visser, C., Visser, P., Fritsche, B., 2018. Torque model verification for the GOCE satellite. Advances in Space Research 62 (5), 1114–1136, doi: 10.1016/j.asr.2018.06.025.

Walker, A., Mehta, P., Koller, J., 2014a. Different implementations of diffuse reflection with incomplete accommodation for drag coefficient modeling. Journal of Spacecraft and Rockets 51 (5), 1522–1532, doi: 10.2514/1.A32668.

Walker, A., Mehta, P., Koller, J., 2014b. Drag coefficient model using the Cercignani–Lampis–Lord gas–surface interaction model. Journal of Spacecraft and Rockets 51 (5), 1544–1563, doi: 10.2514/1.A32677.

Wallace, N., Jameson, P., Saunders, C., Fehringer, M., Edwards, C., Floberghagen, R., 2011. The GOCE ion-propulsion assembly - lessons learnt from the first 22 months of flight operations. In: 32nd International Electric Propulsion Conference, Wiesbaden, Germany. IEPC-2011-327.